Improved Lattice Boltzmann Without Parasitic Currents for Rayleigh-Taylor Instability

Daniele Chiappini[1,*], Gino Bella[1], Sauro Succi[2], Federico Toschi[2,3] and Stefano Ubertini[4]

[1] *University of Rome Tor Vergata, Via del Politecnico 1, I-00133, Rome, Italy.*
[2] *IAC-CNR, Viale del Policlinico 137, I-00161, Rome, Italy.*
[3] *Department of Physics and Department of Mathematics and Computer Science, Eindhoven University of Technology, 5600 MB Eindhoven, The Netherlands.*
[4] *University of Naples Parthenope, Isola C4 - Centro Direzionale, I-80143, Naples, Italy.*

Abstract. Over the last decade the Lattice Boltzmann Method (LBM) has gained significant interest as a numerical solver for multiphase flows. However most of the LB variants proposed to date are still faced with discreteness artifacts in the form of spurious currents around fluid-fluid interfaces. In the recent past, Lee et al. have proposed a new LB scheme, based on a higher order differencing of the non-ideal forces, which appears to virtually free of spurious currents for a number of representative situations. In this paper, we analyze the Lee method and show that, although strictly speaking, it lacks exact mass conservation, in actual simulations, the mass-breaking terms exhibit a self-stabilizing dynamics which leads to their disappearance in the long-term evolution. This property is specifically demonstrated for the case of a moving droplet at low-Weber number, and contrasted with the behaviour of the Shan-Chen model. Furthermore, the Lee scheme is for the first time applied to the problem of gravity-driven Rayleigh-Taylor instability. Direct comparison with literature data for different values of the Reynolds number, shows again satisfactory agreement. A grid-sensitivity study shows that, while large grids are required to converge the fine-scale details, the large-scale features of the flow settle-down at relatively low resolution. We conclude that the Lee method provides a viable technique for the simulation of Rayleigh-Taylor instabilities on a significant parameter range of Reynolds and Weber numbers.

AMS subject classifications: 76T02, 68U02

Key words: Lattice-Boltzmann, multiphase, parasitic currents, Rayleigh-Taylor Instability.

---

*Corresponding author. *Email addresses:* `chiappini@ing.uniroma2.it` (D. Chiappini), `bella@uniroma2.it` (G. Bella), `succi@iac.cnr.it` (S. Succi), `toschi@iac.cnr.it` (F. Toschi), `stefano.ubertini@uniparthenope.it` (S. Ubertini)

1 Introduction

Multiphase flows are ubiquitous in industrial processes (i.e. chemical, pharmaceutical, electronic, and power-generation industries) and natural phenomena alike [1]. Consequently, numerical methods for the investigation of their complex behaviour is in constant demand. However, the task of simulating the behavior of multi-phase flows is very challenging, due to the inherent complexity of the involved phenomena (emergence of moving interfaces with complex topology, droplet collision and break-up), and represents one of the leading edges of computational physics [2, 8]. As a matter of fact, a general computational approach encompassing the full spectrum of complexity exposed by multiphase flows is still not available.

The numerical methods based on the traditional continuum approach (i.e. Navier-Stokes with closure relationships) are usually based on rather complex correlations and often require transient solution algorithms with very small time steps. In the last two decades, a new class of mesoscopic methods, based on minimal lattice formulation of Boltzmann kinetic equation, have gained significant interest as an efficient alternative to continuum methods based on the discretization of the NS equations for non ideal fluids [16].

Since its early days, the Lattice Boltzmann shed promises of becoming a tool for the modeling of multiphase flows. The earliest Lattice Boltzmann simulations of multi-component flows have been performed by Gunstensen et al. [14, 15] and Grunau et al. [16], based on the pioneering Rothman-Keller lattice gas multi-phase model [13]. Ever since, many models have been proposed in order to simulate multiphase flows with the LBM, most of them aiming at incorporating the physics of phase-segregation and interface dynamics, typically hard to model with traditional methods, through simple mesoscopic interaction laws. In particular, the pseudo-potential LBM, due to Shan and Chen [18], has gained increasing popularity on account of its conceptual simplicity and computational efficiency. In the Shan-Chen (SC) method, potential energy interactions are represented through a density-dependent, mean-field, pseudo-potential and phase separation is achieved by imposing a short-range attraction between the light and dense phases. This method allows to track and maintain diffuse interfaces with no need of any special treatment of the interface. However, it is known to present unphysical features (i.e spurious velocities), namely the presence of non-zero velocities even for fluids at rest, with a steady density profile. These spurious currents are disturbing for practical applications, and they may cast doubts on the quantitative accuracy of the simulations methods [28]. The spurious currents have been recently addressed by many authors [3, 4, 17]. He et al. [17] proposed a multi-phase LBM scheme with improved numerical stability. It still incorporates molecular interactions, but unphysical features are alleviated by introducing a pressure distribution function instead of the single-particle density distribution function. A particularly remarkable option has been suggested by Lee et al. [3–6], who proposed a higher order finite difference treatment of the kinetic forces arising from non-ideal interactions (potential energy). In this model, spurious currents are allegedly tamed

by a judicious resort to higher-order finite difference treatment of the non-ideal interactions.

This model is further investigated in the present paper. More specifically, we analyse the conservation properties of the method proposed by Lee et al. [4,5] and show that the spurious currents in the SC model, for the case of a moving droplet at low Weber, result in a distortion of the flow pattern, which is not seen in the simulation with the Lee model. Finally we demonstrate the validity of the scheme for a gravity-driven Rayleigh-Taylor (RT) instability, one of the basic and most demanding problems in the numerical simulation of multiphase flows.

The paper is organized as follows. In Section 2 we briefly review the LB models compared in the present paper. Section 3 presents our numerical results. A side by side comparison between the Lee and the Shan-Chen methods is presented for the case of a static and dynamic droplet. Numerical simulations of the two-dimensional Rayleigh-Taylor instability are then presented and compared with previous numerical results at different Reynolds numbers. Finally in Section 4 conclusions and outlooks are drawn.

2   The models

In this section we present a brief survey of the Lee et al. model [4,5]. As the Shan-Chen [18] has been described at length in many papers, here we only sketch its basic elements.

2.1   The Lee model

The model introduced in [4] starts with a Cahn-Hilliard mixing energy density formulation for an isothermal system [26]. In terms of the composition C, this reads as $E_{mix}(C,\nabla C) = E_0(C) + \frac{\kappa}{2}|\nabla C|^2$, where C is the composition of one component and κ is the gradient parameter. The bulk energy can be rewritten as $E_0(C) \approx \beta C^2(C-1)^2$ where β is a constant fixing the free-energy barrier between the pure states $C=0$ and $C=1$. The same parameter fixes the non-ideal bulk pressure through the (Legendre's) relation:

$$p_0 = C\frac{\partial E_0}{\partial C} - E_0. \tag{2.1}$$

The two free parameters β and κ provide separate control of the surface tension and interface thickness, respectively:

$$\sigma = \frac{\sqrt{2\kappa\beta}}{6}, \quad D = \sqrt{\frac{8\kappa}{\beta}}. \tag{2.2}$$

The external force representing the non-ideal gas effects can be expressed as:

$$\mathbf{F} = \nabla\rho c_s^2 - \nabla p_0 + \rho\kappa\nabla\nabla^2\rho. \tag{2.3}$$

The total pressure in the momentum equation can be obtained by summing to the hydrodynamic pressure p_1, defined later in Eq. (2.15), the thermodynamic pressure p_0 and the curvature term as follows:

$$P = p_0 + p_1 - \kappa C \nabla^2 C + \frac{1}{2}\kappa |\nabla C|^2. \tag{2.4}$$

The Lee model evolves the *pressure* instead of the density, and consequently, the discrete distribution is defined as follows:

$$g_\alpha = f_\alpha c_s^2 + \left(p_1 - \rho c_s^2\right)\Gamma_\alpha(0), \tag{2.5}$$

where f_α is the usual discrete particle distribution, as defined in the classic LBE theory, and $\Gamma_\alpha(\mathbf{u}) = f_\alpha^{eq}/\rho$, and α runs over the set of discrete speeds. In this case the model is written for a two dimensional, nine velocities (D2Q9) LBE.

The total derivative, $D_t = \partial_t + \mathbf{c}_\alpha \cdot \nabla$, of this variable reads as follows:

$$
\begin{aligned}
\frac{\partial g_\alpha}{\partial t} + \mathbf{c}_\alpha \cdot \nabla g_\alpha = &-\frac{1}{\tau}\left(g_\alpha - g_\alpha^{eq}\right) \\
&+ (\mathbf{c}_\alpha - \mathbf{u})\cdot\left[\nabla \rho c_s^2\left(\Gamma_\alpha - \Gamma_\alpha(0)\right) - C\nabla\mu\Gamma_\alpha\right],
\end{aligned} \tag{2.6}
$$

with the following expression for the equilibrium distribution:

$$g_\alpha^{eq} = w_\alpha\left[p_1 + \rho c_s^2\left(\frac{\mathbf{c}_\alpha \cdot \mathbf{u}}{c_s^2} + \frac{(\mathbf{c}_\alpha \cdot \mathbf{u})^2}{2c_s^4} - \frac{(\mathbf{u}\cdot\mathbf{u})}{2c_s^2}\right)\right]. \tag{2.7}$$

The LBE is obtained by discretizing Eq. (2.6) along the characteristics over a timestep δt. Considering the following non-linear transformation [20]:

$$
\begin{aligned}
\bar{g}_\alpha = &g_\alpha + \frac{1}{2\tau}\left(g_\alpha - g_\alpha^{eq}\right) \\
&- \frac{\delta t}{2}(\mathbf{c}_\alpha - \mathbf{u})\cdot\left[\nabla \rho c_s^2\left(\Gamma_\alpha - \Gamma_\alpha(0)\right) - C\nabla\mu\Gamma_\alpha\right],
\end{aligned} \tag{2.8}
$$

$$\bar{g}_\alpha^{eq} = g_\alpha^{eq} - \frac{\delta t}{2}(\mathbf{c}_\alpha - \mathbf{u})\cdot\left[\nabla \rho c_s^2\left(\Gamma_\alpha - \Gamma_\alpha(0)\right) - C\nabla\mu\Gamma_\alpha\right] \tag{2.9}$$

second-order integration in time (Crank-Nicolson), finally leads to the following LBE for pressure field:

$$
\begin{aligned}
&\bar{g}_\alpha\left(\mathbf{x} + \mathbf{c}_\alpha\delta t, t + \delta t\right) - \bar{g}_\alpha\left(\mathbf{x}, t\right) \\
&= -\frac{1}{\tau + 0.5}\left(\bar{g}_\alpha - \bar{g}_\alpha^{eq}\right)(\mathbf{x}, t) + \delta t(\mathbf{c}_\alpha - \mathbf{u})\cdot\left[\nabla \rho c_s^2\left(\Gamma_\alpha - \Gamma_\alpha(0)\right) - C\nabla\mu\Gamma_\alpha\right]_{(\mathbf{x}, t)}.
\end{aligned} \tag{2.10}
$$

The same procedure can be applied to the concentration C, by introducing a second distribution $h_\alpha = (C/\rho)f_\alpha$, $h_\alpha^{eq} = (C/\rho)f_\alpha^{eq}$, which can be shown to obey the following LBE:

$$
\begin{aligned}
\bar{h}_\alpha\left(\mathbf{x} + \mathbf{c}_\alpha\delta t, t + \delta t\right) - \bar{h}_\alpha\left(\mathbf{x}, t\right) = &-\frac{1}{\tau + 0.5}\left(\bar{h}_\alpha - \bar{h}_\alpha^{eq}\right)(\mathbf{x}, t) \\
&+ \delta t(\mathbf{c}_\alpha - \mathbf{u})\cdot\left[\nabla C - \frac{C}{\rho c_s^2}(\nabla p_1 + C\nabla\mu)\right]\Gamma_\alpha|_{(\mathbf{x}, t)} + \delta t\nabla\cdot(M\nabla\mu)\Gamma_\alpha|_{(\mathbf{x}, t)},
\end{aligned} \tag{2.11}
$$

where the modified equilibrium distribution $\bar{h}_\alpha$ and its equilibrium are calculated as in (2.8) and (2.9), namely:

$$\bar{h}_\alpha^{eq} = h_\alpha^{eq} - \frac{\delta t}{2}(\mathbf{c}_\alpha - \mathbf{u}) \cdot \left[\nabla C - \frac{C}{\rho c_s^2}(\nabla p_1 + C\nabla\mu)\right]\Gamma_\alpha|_{(\mathbf{x},t)}$$
$$- \frac{\delta t}{2}\nabla\cdot(M\nabla\mu)\Gamma_\alpha|_{(\mathbf{x},t)}. \tag{2.12}$$

In the above M is the mobility, a chemical factor which rules the velocity of the convergence to the equilibrium. In Lee's work [4] it is shown that spurious currents decrease rapidly as M is increased.

The composition, the hydrodynamic pressure and the momentum are calculated by taking the zeroth and the first moments of the modified particle distribution function:

$$C = \sum_\alpha \bar{h}_\alpha + \frac{\delta t}{2}\nabla\cdot(M\nabla\mu), \tag{2.13}$$

$$\rho c_s^2 \mathbf{u} = \sum_\alpha \mathbf{c}_\alpha \bar{g}_\alpha - \frac{\delta t}{2}C\nabla\mu, \tag{2.14}$$

$$p_1 = \sum_\alpha \bar{g}_\alpha + \frac{\delta t}{2}\mathbf{u}\cdot\nabla\rho c_s^2. \tag{2.15}$$

Eq. (2.13) is non linear, because the equilibrium chemical potential μ is a function of the composition C. This means that, in principle, μ should be obtained by solving the nonlinear equation $\mu = \mu(C)$ by iteration at each lattice site. However, due to the slow variation of the chemical potential on the time-scale of a single time-step, in our implementation, C at time t is updated with the value of μ at the previous time-step $t-\delta t$, as suggested in [6]. The density and the relaxation time are calculated as local functions of the composition

$$\rho(C) = C\rho_1 + (1-C)\rho_2,$$
$$\tau(C) = C\tau_1 + (1-C)\tau_2. \tag{2.16}$$

The additional terms proportional to δt in Eqs. (2.13), (2.14) and (2.15), are introduced in order to cancel the contribution of the forces to the mass conservation.

2.2 The discretization of the Lee model

Crucial to the successful implementation of the Lee model is the proper discretization of the forcing terms:

$$F_\alpha^{(g)} = (\mathbf{c}_\alpha - \mathbf{u}) \cdot \left[\nabla\rho c_s^2(\Gamma_\alpha - \Gamma_\alpha(0)) - C\nabla\mu\Gamma_\alpha\right]_{(\mathbf{x},t)},$$
$$F\alpha^{(h)} = (\mathbf{c}_\alpha - \mathbf{u}) \cdot \left[\nabla C - \frac{C}{\rho c_s^2}(\nabla p_1 + C\nabla\mu)\right]\Gamma_\alpha|_{(\mathbf{x},t)} + \nabla\cdot(M\nabla\mu)\Gamma_\alpha|_{(\mathbf{x},t)}. \tag{2.17}$$

Both terms are prefactored by the peculiar velocities $\mathbf{c}_\alpha - \mathbf{u}$, which, once summed upon over all discrete speeds, automatically cancel, as it is appropriate for a mass-conserving term. *However, this property is broken by the Lee discretization.* To appreciate this point, let us rewrite both forces as the sum of separate pieces, moving along the molecular and fluid speed directions, respectively

$$
\begin{aligned}
F_\alpha^{(g)} &= \mathbf{c}_\alpha \cdot \nabla A \Gamma_\alpha - \mathbf{u} \cdot \nabla A \Gamma_\alpha, \\
F_\alpha^{(h)} &= \mathbf{c}_\alpha \cdot \nabla B \Gamma_\alpha - \mathbf{u} \cdot \nabla B \Gamma_\alpha + \nabla \cdot (M \nabla \mu) \Gamma_\alpha.
\end{aligned}
\tag{2.18}
$$

In the above, A and B represent generic space-time dependent quantities to be discretized.

The term corresponding to the microscopic velocity is discretized along the characteristics, instead the other one, corresponding to the macroscopic velocity, is discretized using standard gradients ([4] and Lee private communication).

The gradient along the characteristics which approximates $\mathbf{c}_\alpha \cdot \nabla A$ can be expanded to the first and second order, respectively, as follows:

$$
\mathbf{c}_\alpha \cdot \nabla A|_{(\mathbf{x},t)} = \frac{A(\mathbf{x}+\mathbf{c}_\alpha \delta t) - A(\mathbf{x}-\mathbf{c}_\alpha \delta t)}{2},
\tag{2.19}
$$

$$
\mathbf{c}_\alpha \cdot \nabla A|_{(\mathbf{x},t)} = \frac{5A(\mathbf{x}+\mathbf{c}_\alpha \delta t) - 3A(\mathbf{x}) - A(\mathbf{x}+2\mathbf{c}_\alpha \delta t) - A(\mathbf{x}-\mathbf{c}_\alpha \delta t)}{4}.
\tag{2.20}
$$

The same approximation is used for the other forcing term $\mathbf{c}_\alpha \cdot \nabla C \Gamma_\alpha$.

It should be noticed that each different direction leads to a separate discretization stencil, i.e. it is a Lagrangian discretization along the characteristics defined by the discrete velocities.

The standard (non-Lagrangian) discretization consists of two different gradients, the first-order centered and the second-order biased, respectively:

$$
\begin{aligned}
\nabla^C A|_{(x)} &= \sum_{\alpha \neq 0} \frac{w_\alpha \mathbf{c}_\alpha [A(\mathbf{x}+\mathbf{c}_\alpha \delta t) - A(\mathbf{x}-\mathbf{c}_\alpha \delta t)]}{2c_s^2 \delta t}, \\
\nabla^B A|_{(x)} &= \sum_{\alpha \neq 0} \frac{w_\alpha \mathbf{c}_\alpha [-A(\mathbf{x}+2\mathbf{c}_\alpha \delta t) + 4A(\mathbf{x}+\mathbf{c}_\alpha \delta t) - 3A(\mathbf{x})]}{2c_2^2 \delta t}.
\end{aligned}
\tag{2.21}
$$

The use of a second order is necessary to ensure the stability to the method. In the different phases of the simulation, the first order approximation is used for the forcing term of the equilibrium distributions defined in Eqs. (2.9) and (2.12), the second order is used for the force applied to the collision operators of Eqs. (2.10) and (2.11).

By writing the discretized forcing terms for each population and summing up all contributions, it is possible to demonstrate that this method is numerically non-conservative. In fact, using only a first order approximation, the method is completely conservative, but in the collision phase there appears a spurious contribution due to the imbalance between the finite differencing over the characteristics and the local fluid direction. The

main problem is that the coefficients in the second order discretization are different between the flow gradient and the one evaluated along the characteristics. In fact, if these coefficients were equal, the local contribution of this "hybrid" discretization would be zero.

For example, assuming the forcing term written as in Eq. (2.18), the spurious non-conservative contribution of the global forcing is obtained by summing the correction terms over all the populations:

$$
\begin{aligned}
\sum_\alpha F_\alpha^{(h)} = & -\frac{3}{4}B(i,j)\sum_{\alpha=1}^{8}\Gamma_\alpha \\
& +B(i+1,j)\left[\frac{5}{4}\Gamma_1-\frac{1}{4}\Gamma_3-\frac{2uw_1}{c_s^2}\right]+B(i-1,j)\left[\frac{5}{4}\Gamma_3-\frac{1}{4}\Gamma_1+\frac{2uw_3}{c_s^2}\right] \\
& +B(i+2,j)\left[-\frac{1}{4}\Gamma_1+\frac{uw_1}{2c_s^2}\right]+B(i-2,j)\left[-\frac{1}{4}\Gamma_3-\frac{uw_3}{2c_s^2}\right] \\
& +B(i,j+1)\left[\frac{5}{4}\Gamma_2-\frac{1}{4}\Gamma_4-\frac{2vw_2}{c_s^2}\right]+B(i,j-1)\left[\frac{5}{4}\Gamma_4-\frac{1}{4}\Gamma_2+\frac{2vw_4}{c_s^2}\right] \\
& +B(i,j+2)\left[-\frac{1}{4}\Gamma_2+\frac{vw_2}{2c_s^2}\right]+B(i,j-2)\left[-\frac{1}{4}\Gamma_4-\frac{vw_4}{2c_s^2}\right] \\
& +B(i+1,j+1)\left[\frac{5}{4}\Gamma_5-\frac{1}{4}\Gamma_7-\frac{2(u+v)w_5}{c_s^2}\right] \\
& +B(i-1,j-1)\left[\frac{5}{4}\Gamma_7-\frac{1}{4}\Gamma_5+\frac{2(u+v)w_7}{c_s^2}\right] \\
& +B(i+2,j+2)\left[-\frac{1}{4}\Gamma_5-\frac{(u+v)w_5}{2c_s^2}\right] \\
& +B(i-2,j-2)\left[-\frac{1}{4}\Gamma_7+\frac{(u+v)w_7}{2c_s^2}\right] \\
& +B(i-1,j+1)\left[\frac{5}{4}\Gamma_6-\frac{1}{4}\Gamma_8+\frac{2(u-v)w_6}{c_s^2}\right] \\
& +B(i+1,j-1)\left[\frac{5}{4}\Gamma_8-\frac{1}{4}\Gamma_6-\frac{2(u-v)w_8}{c_s^2}\right] \\
& +B(i-2,j+2)\left[-\frac{1}{4}\Gamma_6+\frac{(u-v)w_6}{2c_s^2}\right] \\
& +B(i+2,j-2)\left[-\frac{1}{4}\Gamma_8-\frac{(u-v)w_8}{2c_s^2}\right] \\
& +\nabla(M\cdot\nabla\mu).
\end{aligned}
\tag{2.22}
$$

We notice that the last term, with the second order derivative is not expanded because it cancels out in the Eq. (2.13). It is important to underline that this discretization is non-conservative, as some terms in the local force are different from zero. In particular, the

discretization is conservative for the case of no-flow ($u\!=\!v\!=\!0.0$) and/or A and B are trivially constant. Nevertheless, simulation practice shows that the non-conservative term, although non-zero at each lattice site, particularly near the interface, does not appreciably perturb the actual solution. Moreover the total mass (sum over all lattice sites) is conserved. Similar considerations apply to the fluid momentum, whose lack of conservation might have implications on the Galilean invariance of the model. This remains as a standing issue for future investigations of the properties of the Lee's model.

2.3 The Shan Chen Model

The Shan-Chen model [18] is based on the following expression for the non-ideal force:

$$\mathbf{F}(\mathbf{x},t) = -G_0 \psi(\mathbf{x},t) \sum_{\alpha}^{N_{pop}} \psi(\mathbf{x}+\mathbf{c}_\alpha \Delta t,t) \mathbf{c}_\alpha w_\alpha, \tag{2.23}$$

where N_{pop} is the number of possible directions in every lattice site (9 in this approach) and $\psi(\mathbf{x},t)$ is a local functional of a density:

$$\psi(\mathbf{x},t) = \rho_0 \left[1 - \exp\left(-\frac{\rho(\mathbf{x},t)}{\rho_0} \right) \right]. \tag{2.24}$$

In this application the reference density ρ_0 is set to $\rho_0\!=\!1$ and G_0 is the basic parameter which rules the inter-particle interaction. In this model, G_0 is the only free parameter fixing both density ratio and the surface tension of the model. The possibility of modifying these values is limited to a short range of values near the equilibrium ones.

Starting from Eq. (2.23) the component of the interaction potential along each direction can be evaluated. This force is used for shifting the velocities prior to evaluating the equilibrium distribution functions, according to:

$$\mathbf{u}'(\mathbf{x},t) = \mathbf{u}(\mathbf{x},t) + \frac{\mathbf{F}(\mathbf{x},t)\tau}{\rho(\mathbf{x},t)}. \tag{2.25}$$

The Equation of State of the system is influenced by this contribution, and takes the following form:

$$P = p_0 + \frac{c_s^2 G_0}{2} \psi^2 = \rho c_s^2 + \frac{c_s^2 G_0}{2} \psi^2. \tag{2.26}$$

As evident from the previous equations, the Shan-Chen is significantly simpler than Lee's model. Spurious currents, and a relatively narrow range of liquid/gas density ratios are the price of this simplicity.

Modern variants [21–23] considerably extend the scope of the SC model, but in the sequel we shall refer to the standard version.

3   Results

3.1   The static drop

As the first test case, a two dimensional static drop is chosen, in order to highlight the drastic reduction of spurious currents achieved by the Lee versus SC model.

A drop of liquid with radius $R = 25$ is initialized in the centre of a fully periodic box, being the interface thickness D equal to 4 lattice sites. The density ratio between liquid and vapor phases $\rho_l^{sat}/\rho_v^{sat}$ is set to 1000. The simulation is stopped when the kinetic energy, defined as

$$KE = \sum_{domain} \frac{(u^2 + v^2)}{2},$$

becomes practically constant.

Fig. 1 shows that KE is constantly decreasing until its minimum value, reached after about 4×10^5 iterations, and then remains nearly constant for the following 6×10^5 iterations.
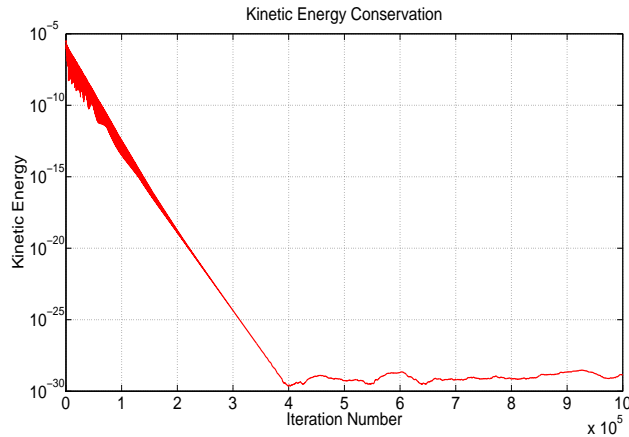
Figure 1: Time evolution of the kinetic energy for the case of a static drop. After 4×10^5 the kinetic energy reaches value near the round-off precision of the machine and remains practically constant. The main parameters are: $R = 25$, $\rho_l^{sat}/\rho_v^{sat} = 1000.0, \tau_v/\tau_l = 10.0$. The grid resolution is 100×100.

The non-conservative effect of the discretization is apparent from Fig. 2, which shows the distribution of the local force, summed over all the populations (Eq. (2.11)). However, the non-conservative term of the forcing, still present in the lattice sites of the interface zone (black line in Fig. 2), has negligible effects on the total mass variation, as shown in Fig. 3.

3.2   The dynamic drop – A comparison with the Shan-Chen model

In this section a comparison between the Lee model and the Shan-Chen model is performed. These two models differ considerably from each other and, consequently, their
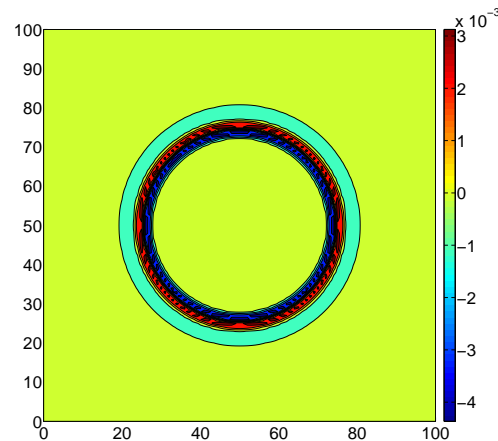
Figure 2: Contour plot of the spurious force after the collision phase, evaluated after 10^6 time-steps. As expected, the spurious force is peaked around the interface. The main parameters are: $R = 25$, $\frac{\rho_l^{sat}}{\rho_v^{sat}} = 1000.0, \frac{\tau_v}{\tau_l} = 10.0$. The grid resolution is 100×100.
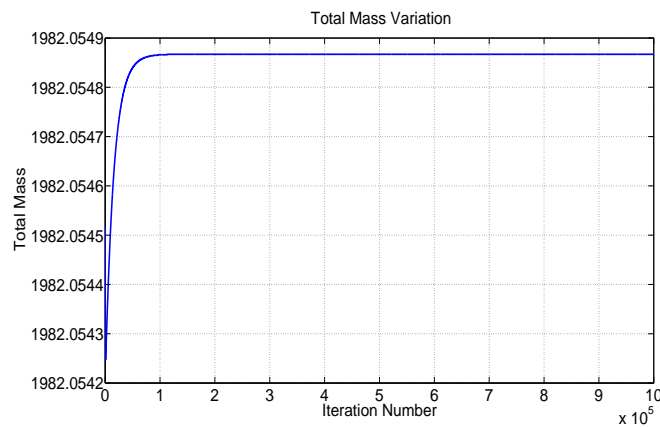
Figure 3: Conservation of the total mass for the static drop. As expected the spurious force has no effect on the value of the total mass. The main parameters are: $R = 25$, $\frac{\rho_l^{sat}}{\rho_v^{sat}} = 1000.0, \frac{\tau_v}{\tau_l} = 10.0$. The grid resolution is 100×100.

range of applicability are also quite distinct, which makes a quantitative comparison rather non-trivial. The Lee model describes a Van der Waals fluid with two free parameters, κ and β, and consequently it allows a separate tuning of the density ratio and the surface tension. The Shan-Chen model, on the other hand, takes into account only the interaction potential, which fixes both the dense to light phase density ratio and the surface tension. In addition the SC method tends to produce comparatively high values of the surface tension, as phase-separation is achieved only above a critical threshold $|G| > G_{crit} = 4$, and the surface tension scales proportionally to $|G|$. Moreover, once the coupling strength G_0 is fixed, the density ratio and the surface tension are automatically

imposed. More specifically, with concern to the surface tension, the standard SC scheme operates in a regime of $\sigma \sim 0.01 - 0.1$ (lattice units). Smaller values would entail very small density ratios because, as mentioned above, the same parameter G controls both surface tension and the non-ideal pressure. Larger values, on the other hand, run against problems of numerical stability triggered by strong interface forces. In the Lee's model, the surface tension is generally about one order of magnitude below the SC value. Indeed, values of $\sigma > 0.01$ are typically found to generate numerical instabilities due to large interface forces. The factor ten between the two methods is likely to be due to the major difference in the discretization of the non-ideal interactions, which requires second-oder neighbors in the Lee's method and only first-order neighbors in the standard SC method (the situation would be different for multi-range SC methods, which allow considerably smaller values of σ), [22–25]. The main advantage of achieving low surface tensions is the possibility to simulate higher Weber numbers at a given grid resolution. As to the density ratio, the standard SC model is usually limited to values $\mathcal{O}(100)$, whereas the Lee's model can easily reach up to $\mathcal{O}(1000)$. This is again due to the fact that in the latter, the density ratio is independent of the surface tension. Thus, the Lee's method appears more suited to applications involving large density ratios between the dense and light fluid (say water/air mixtures). Finally, as to the kinematic viscosity, ν, although the two schemes are based on a different time-marching procedure, leading to $\nu = c_s^2(\tau - 1/2)$ for SC and $\nu = c_s^2 \tau$ for Lee, generally they are both operated in a moderately high-viscous regime, $\nu \sim 0.1$ (lattice units), which is adequate for a large variety of multiphase flows at moderate Reynolds numbers. Clearly, the broader applicability of the Lee's method, has to be weighted against a higher complexity and computational demand as compared to the SC method. The above considerations clarify the limitations in identifying an overlapping region between the models. However, after a series of preliminary tests, it was found that a comparison can be established for $G_0 = -4.3$, which is close to the separation limit. The resulting density ratio and the surface tension are:

$$\rho_{liquid} = 1.29;$$
$$\rho_{gas} = 0.33; \quad\quad\quad\quad\quad\quad\quad\quad\quad\quad (3.1)$$
$$\sigma = 0.0104.$$

To calibrate the Lee model in order to obtain the same σ and density ratio, the parameter β has been tuned in Eq. (2.2), by imposing a constant interface thickness $D = 4$. Starting from Eq. (2.2), the parameter β is evaluated as:

$$\beta = \frac{12\sigma}{D} = 0.0312. \quad\quad\quad\quad\quad\quad\quad\quad (3.2)$$

Droplet deformation by aerodynamic forces is a complex flow phenomenon in which the non-homogeneous pressure distribution on the surface of the bubble leads to shape deformation and then to droplet breakup. Deformation and breakup of a liquid droplet by aerodynamic forces is usually classified through the dimensionless Weber number,

(a) Lee   (b) ShanChen
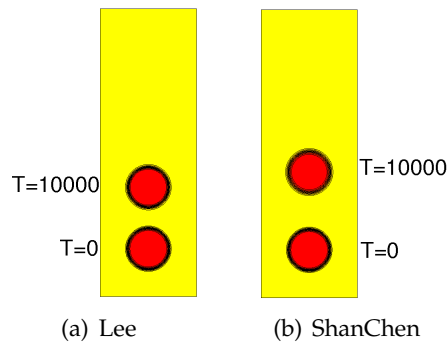
Figure 4: Comparison between Shan-Chen and Lee models. Density contours at the beginning and at the end of the simulation. The main differences are the distance covered by the two drops and the interface thickness, which remains constant in the Lee model. Parameters of the simulation are $We_0 = 3$, $\sigma = 0.0104$, $R = 20$.

(a) Lee - Vector   (b) Shan Chen   (c) Shan   Chen -
                     - Vector   Relative   Velocity
                                       (see text)
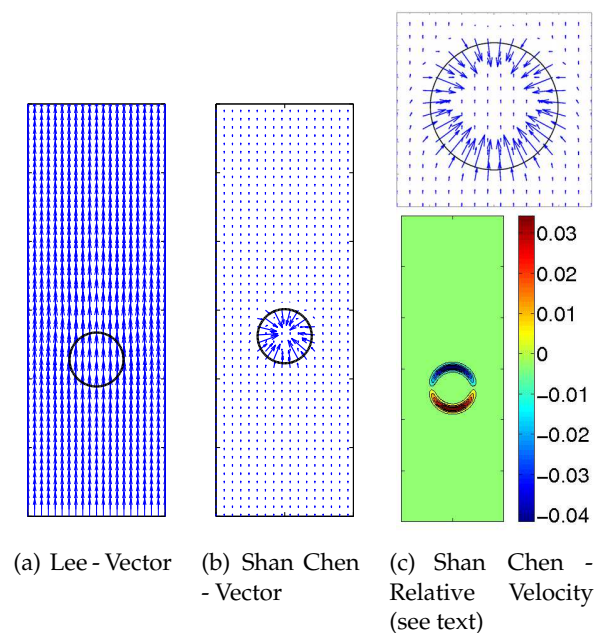
Figure 5: Comparison between Shan-Chen and Lee models. Vector and asymptotic velocity at the end of the simulation (time-step 10000). The main parameters of the simulation are $We_0 = 3$, $\sigma = 0.0104$, $R = 20$. On top of panel 5(c), shown is the blow-up of the velocity field near the interface. The lower panel shows the relative velocity (see text).

which defines the ratio between the inertia and the surface tension forces:

$$We = \frac{\rho_{gas} U^2 D_C}{\sigma},$$ (3.3)

where D_C is the characteristic length of the system (i.e. the droplet diameter).

A rectangular box with 100 lattice sites in the x-direction and 300 in the y-direction is used as computational domain and a two dimensional circular liquid drop with $R = 20$

is initialized, with its center located 50 lattice sites from the inlet in the y-dimension and in the center of the other dimension. The initial droplet velocity is set to 0.0486 lattice units, which corresponds to $We_0 = 3$, sufficiently small to avoid drop deformation during the simulation. Fig. 4 shows a comparison of the density contours calculated by the two models at the beginning and after 10,000 iterations. Two main differences can be identified. First in the SC case the droplet lies ahead. This is due to a different behaviour in the initial stage of evolution, although the asymptotic speed is the same. Second, the interface thickness, constantly equal to four lattice units in the Lee model, increases up to six grid-points with the SC model.

The velocity vectors after 10,000 iterations shown in Figs. 5(a) and 5(b) highlight that the Lee model yields a perfectly uniform and aligned velocity field, as it should be at steady-state, while in the SC model, a flow rate across the interface (i.e. spurious currents) is observed. The parasitic currents are also evident in Fig. 5(c), which shows the relative velocity $V_{rel} = V - v_\infty$, where v_∞ is the flow velocity far from the interface.

The relative velocity for the Lee model is not reported because the value of V_{rel} is uniform and almost zero all over the domain (two orders of magnitude below the V_{rel} calculated with the SC). A quantitative comparison between the two methods is non-trivial due to the basic differences between the two formulations of the intermolecular interactions. For instance, we have observed that the Lee interaction takes longer to settle to a steady-state configuration. Apart from these differences, it is clear that in the long-term, the Lee model correctly reproduces a situation where the droplet moves at the same velocity as the surrounding fluid. This confirms that spurious terms are under a better control as compared with the Shan-Chen model.

3.3　The Rayleigh-Taylor instability

Next, we test the Lee model against a gravity-driven Rayleigh-Taylor (RT) instability, one of the most fundamental forms of interfacial instability between fluids of different densities, which has been extensively studied both numerically and experimentally [27].

The computational domain is a channel of width $W = 100$ and a height $H = 4W$. Symmetric boundary conditions are applied on the top and bottom wall and periodic boundary conditions are imposed at the side walls. The heavier fluid, initially placed above the lighter one, falls down under the effect of the gravity field when the interface is perturbed. Subsequently, as the heavy fluid moves downwards, a wave-like disturbance appears at the interface. Downward-moving 'spikes' and upward-moving 'bubbles' are observed. The initial perturbation of the interface is a sinusoidal function, with amplitude $A = 0.1W$ and wavelength $\lambda = 2\pi/W$. Being g the gravity acceleration in lattice units, the characteristic velocity of the system is $U = \sqrt{W \cdot g}$, which has been set to 0.04 for all the simulations. The Lee model has been tested under different operating conditions, given in terms of non-dimensional parameters. The Reynolds number is defined as: $Re = \sqrt{Wg}W/\nu$ where ν is the fluid viscosity. The density ratio is measured in terms of the Atwood number, defined as: $At = (\rho_l - \rho_g)/\rho_l + \rho_g$ with ρ_l and ρ_g being the den-
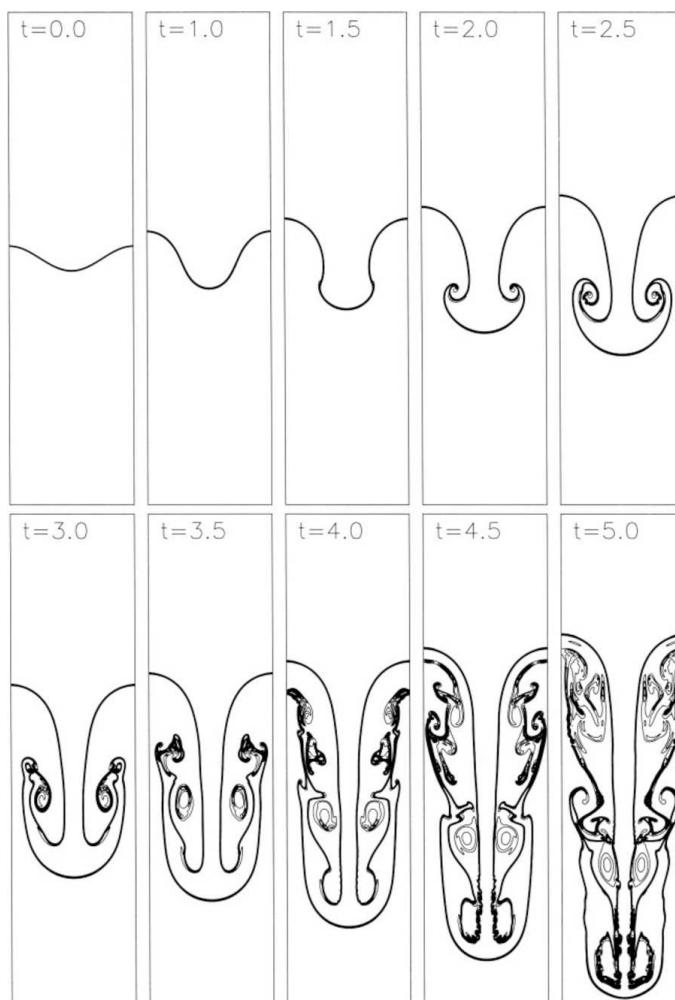
Figure 6: A sequence of density contours for the RT instability at different times, as presented in the reference [12]. The main parameters are: grid-size 256x1024, Re = 2048, At = 0.5 and $\sqrt{W \cdot g} = 0.04$.

sities of the light and heavy fluids, respectively. The natural time-scale of the system is given by $T = \sqrt{W/g}$.

In order to assess the validity of the model, the present numerical results are compared with those obtained by He et al. [12]. The comparison has been performed for two different cases: a 256x1024 grid, with Re = 2048 and At = 0.5; a 128x512 grid, with Re=256 and At=0.5.

Figs. 6 and 7 show the evolution of the fluid interface from He et al. [12] and from the Lee model, respectively, at a $Re = 2048$. The agreement with literature results is satisfactory. The flow field is qualitatively consistent with the typical RT instability dynamics, experimentally and numerically observed by various authors [7, 29–33]: the initial expo-

(a) t = 0.0   (b) t = 1.0   (c) t = 1.5   (d) t = 2.0   (e) t = 2.5

(f) t = 3.0   (g) t = 3.5   (h) t = 4.0   (i) t = 4.5   (j) t = 5.0
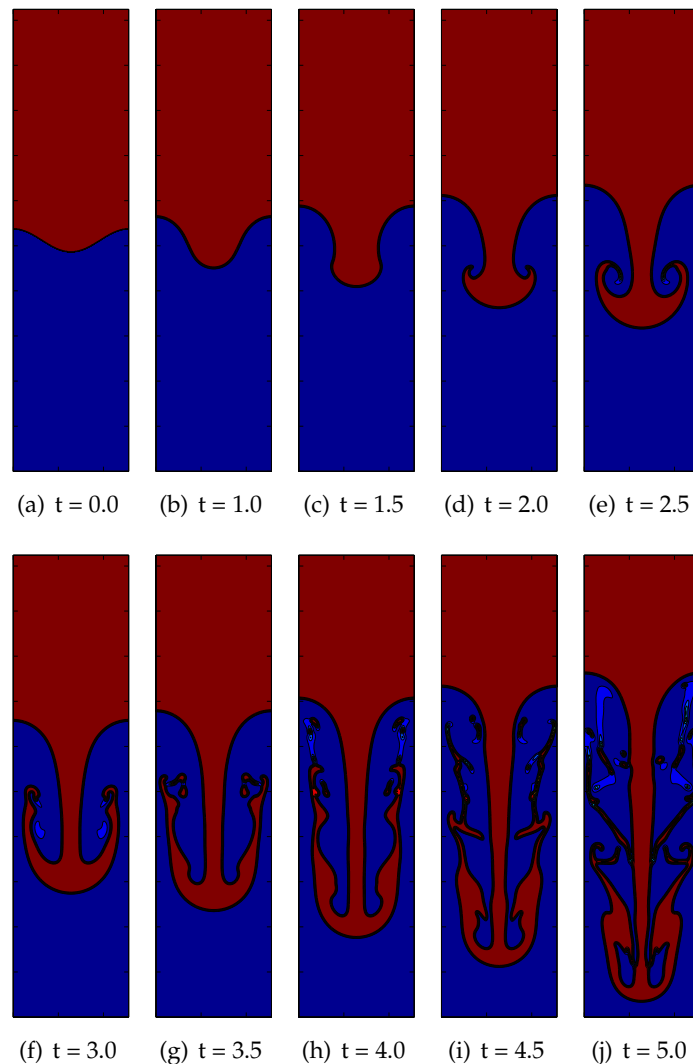
Figure 7: A sequence of density contours for the RT instability at different times, as computed with the Lee's model. The main parameters are: grid-size 256x1024, Re = 2048, At = 0.5 and $\sqrt{W \cdot g} = 0.04$.

nential growth, the rise bubble of the light fluid and the spikes of denser fluid moving in the opposite direction as well as the superficial wave breaking at a later stage of the simulation, are well visible.

A better insight is obtained by monitoring the evolution of the interface at low and high Re, shown in Fig. 8, which reveals significant differences at $t = 3T$. These are mainly related to the dense jet breakup: at high Re, more and smaller dense fluid elements separate from the main jet. A quantitative comparison with the literature data in terms of the spike and bubble leading front positions is given in Fig. 9. Again, satisfactory agree-
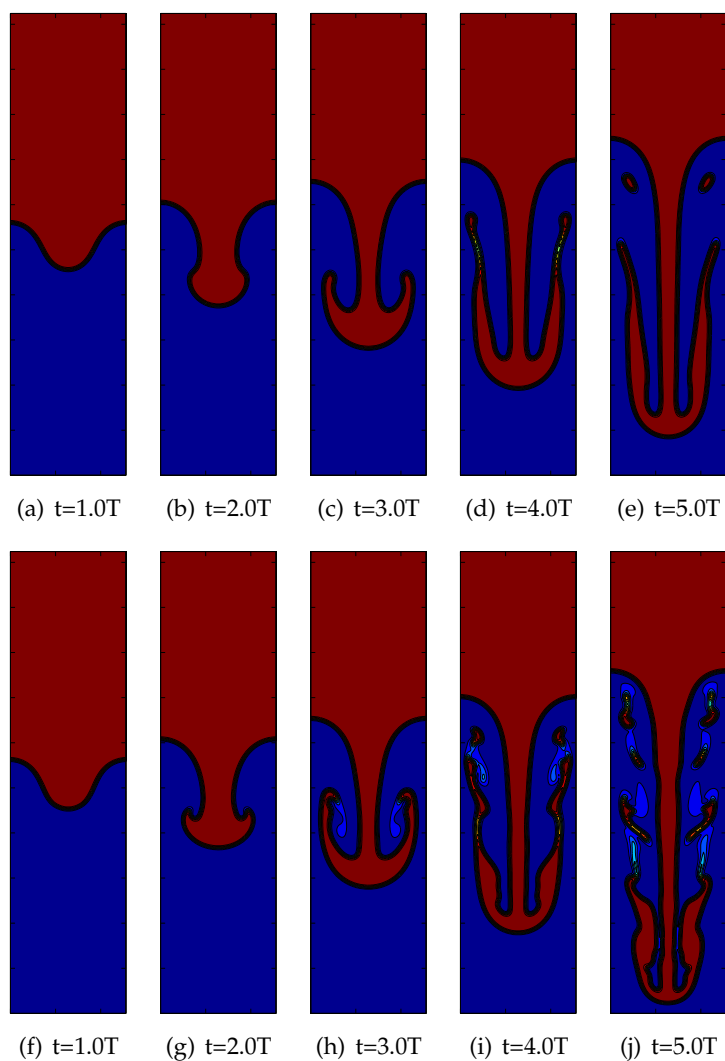
Figure 8: A sequence of density contours at different times as computed with the Lee's model - Two different Re are examined: 1)Re = 256 figure 8(a) to 8(e); 2)Re = 2048 figs 8(f) to 8(j). Other parameters are: Grid size = 128 × 512, $At = 0.5$, $\sqrt{W \cdot g} = 0.04$.

ment between our results and literature data is observed. Fig. 9 reveals that the evolution of the global parameters is only marginally affected by the Reynolds number, as small differences are observed only at a later stage of the simulations.

3.4 Lack of mass conservation

Inspection of mass-conservation for the RT instability (see Fig. 10), shows indeed a deterioration with respect to the case of a static droplet shown previously in this work. From
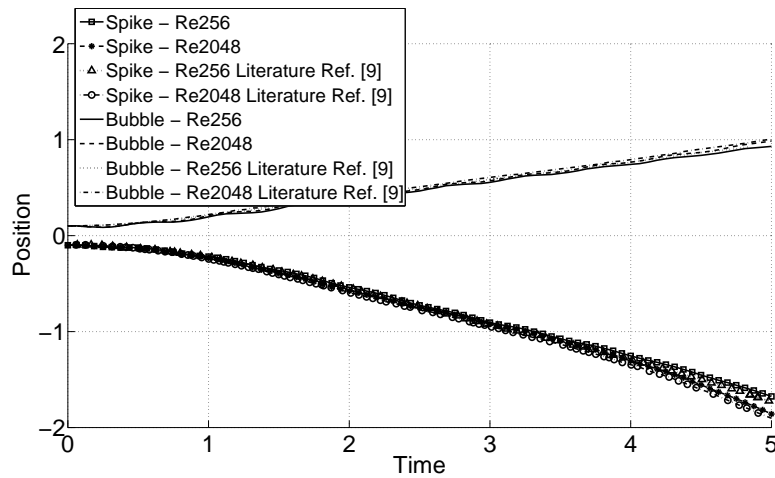
Figure 9: Position of the spike and bubble as a function of time. Comparison between the Lee's model and the literature data [12] for two different Re numbers. The main parameters are: grid size = 128 × 512, At = 0.5, $\sqrt{W \cdot g}$ = 0.04. The examined Re number are 256 and 2048.
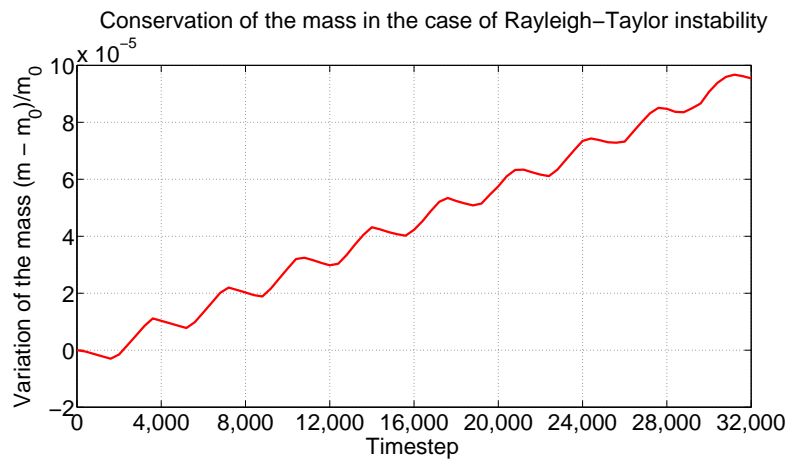
Figure 10: Conservation of the total mass for the Rayleigh-Taylor Instability. The variation of the mass respect to the initial condition is reported. The parameters of the simulation are Re = 2048, grid size = 256 × 1024, At = 0.5, $\sqrt{W \cdot g}$ = 0.04.

Fig. 10), it is seen that the relative mass non-conservation reaches up to 10^{-4} after 32,000 timesteps, with a linear growth rate of about 10^{-8} per time step. Besides unsteadiness, which is inherent to the RT instability, this error growth could be related also to the effect of symmetric boundary conditions on the north/south walls. The development of optimal boundary conditions for the Lee model is an open research topic, which deserves a full study on its own. Nevertheless, we notice that for the test cases presented in this work, the error due to mass non-conservation appears to be sufficiently low to preserve the essential physics of the problem.
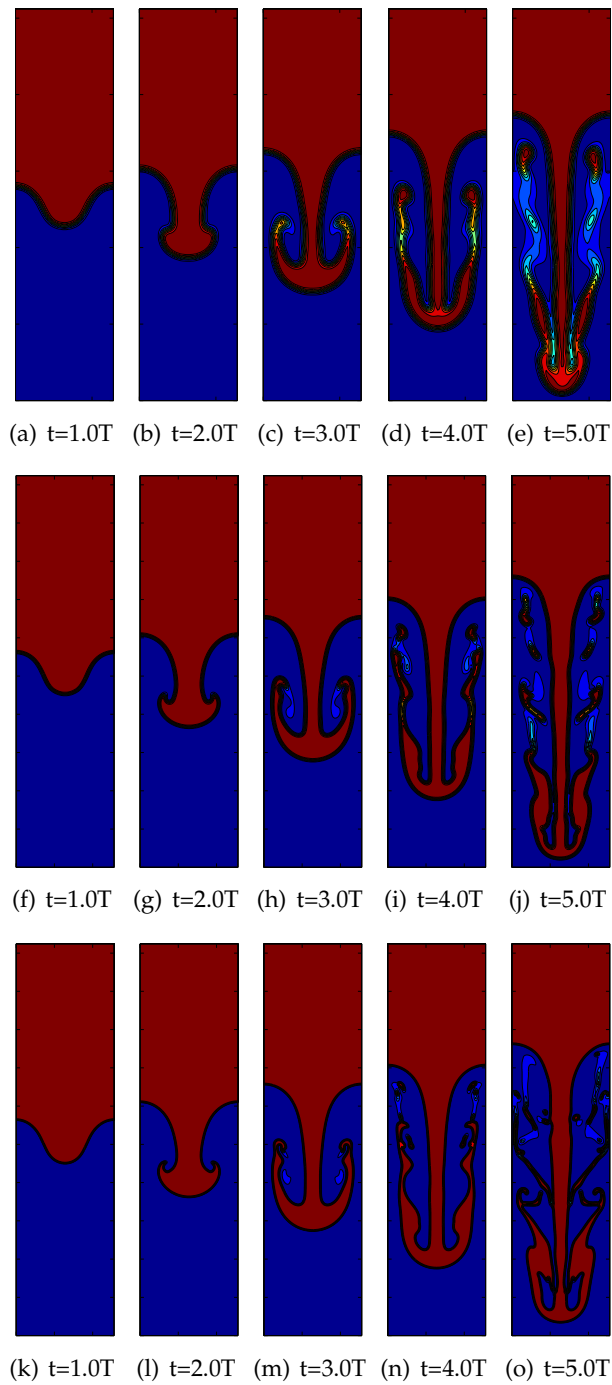
Figure 11: Grid Size effects. A sequence of density contours of RT instability at different times, as computed with the Lee's model with different grids - Three different grids are examined: 1) 64x256 panels 11(a) to 11(e); 2) 128x512 panels 11(f) to 11(j); 3) 256x1024 panels 11(k) to 11(o). Other parameters are: $Re = 2048$, $At = 0.5$, $\sqrt{W \cdot g} = 0.04$.
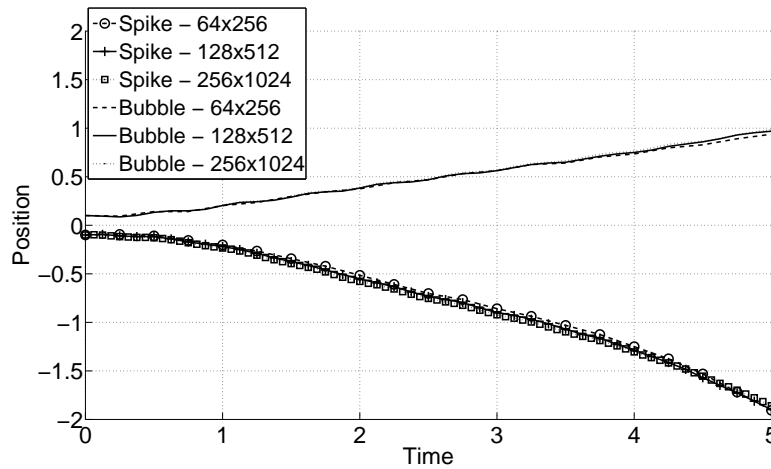
Figure 12: Grid Size effects on the evolution of the penetration of the bubble and the spike. No apparent differences can be appreciated for these "global" quantities. The main differences are shown in the previous figure, which shows the density contours at different times. Parameters: Re = 2048, At = 0.5 and $\sqrt{W \cdot g}$=0.04. - Three different grids are examined: 64×256, 128×512 and 256×1024.

3.5   Effect of the grid-size

The gravity-driven RT instability has been simulated at three different resolutions: 64×256; 128×512 and 256×1024. The Reynolds and Atwood numbers have been set to 2048 and 0.5, respectively. As can be observed in Fig. 11, which compares the fluid interface evolution with the different grids, the grid-resolution significantly affects the interface dynamics. The difference between the finest and the coarsest grids is evident at any stage of the RT instability growth, as the interface shape and the spike penetration are clearly different already at $t = 2T$.

   The effectiveness of the grid refinement, from 128×512 to 256×1024, becomes more apparent as the fluid interpenetration becomes turbulent and the scale of the wave disturbances becomes smaller. Since a coarser grid inevitably implies a larger interface thickness, liquid breakup is brought forward by the coarser grids, as well as the separated structures are smaller with the finest grid. Passing from the 128×512 to the 256×1024 grids, the differences in the jet shape become apparent only after 5T, a time at which the relevant scales of the flow have become smaller.

   The differences are much less evident at the level of the main penetration parameters. The time evolutions of the falling spike and the rear bubble position are almost the same for the three grids, as shown in Fig. 11.

4   Conclusions

In this paper we have presented an investigation of the model proposed by Lee et al. [4,5], which tames spurious currents by a higher order finite-differencing treatment of non-

ideal forces. The comparison with the SC model for a moving low Weber droplet shows that the Lee model is free of numerical artifacts, such as spurious currents arising in the wake of the droplet. The simulations also highlight that with the Lee model the interface thickness keeps the same value all along the simulation, while in the SC a slow increase in time is observed (i.e. from four to six lattice units).

The method has been quantitatively validated against previous numerical results on two-dimensional Rayleigh-Taylor instabilities at different Reynolds numbers and grid resolutions. The computed flow field is qualitatively consistent with the complex RT instability dynamics previously observed in experimental studies, and the agreement between our results and literature data is very satisfactory in terms of spike and bubble leading front positions. It is also shown that the Reynolds number, in the range 256-2048, has significant effects only at a late stage, when jet breakup occurs. Finally, we show that the lattice spacing plays a significant role on the interface dynamics. The differences between the coarse and the fine grids (64×256 vs 256×1024) become more evident as the fluid interpenetration proceeds towards the generation of small scale disturbances.

In this study we also analytically demonstrate that the Lee model is in principle non conservative, due to the different discretization of the streaming operator along the direction of molecular versus fluid motion. However, numerical practice shows that this lack of conservation produces negligible effects, at least for the cases shown in this paper. This property, so far un-noticed to the best of our knowledge, is key to the practical success of the method.

Acknowledgments

References

[1] M. Ishii and T. Hibiki, Thermo-Fluid Dynamics of Two-Phase flow, Springer, 2007.
[2] A. Prosperetti and G. Tryggvason, Computational Methods for Multiphase Flow, Cambridge University Press, 2005.
[3] T. Lee and C.-L. Lin, A stable discretization of the lattice Boltzmann equation for simulation of incompressible two-phase flows at high density ratio, Journal of Computational Physics 206 (2005) 16-47.
[4] T. Lee and P. F. Fischer, Eliminating parasitic currents in the lattice Boltzmann equation method for nonideal gasses, Phys. Rev. E 74 (2006) 046709.
[5] T. Lee, Effects of incompressibility on the elimination of parasitic currents in the lattice Boltzmann equation method for binary fluids, Computers and Mathematics with Applications (2009), doi:10.1016/j.camwa.2009.02.017
[6] T. Lee and L. Liu, Wall boundary condition in the lattice Boltzmann equation method for nonideal gasses, Phys. Rev. E 78 (2008) 017702.

[7] R. R. Nourgaliev, T. N. Dinh and T. G. Theofanous, A pseudocompressibility method for the numerical simulation of incompressible multifluid flows, International Journal of Multiphase Flow 30 (2004) 901-937.

[8] S. Zaleski, J. Li and S. Succi, Two-dimensional Navier-Stokes simulation of deformation and breakup of liquid patches, Phys. Rev. Lett. 75 (1995) 244-247.

[9] B. J. Daly, Numerical study of two fluid Rayleigh-Taylor instability, Phys. Fluids 10 (1967) 297-307.

[10] D. L. Youngs, Numerical simulation of turbulent mixing by Rayleigh-Taylor instability, Physica D 12 (1984) 32-44.

[11] G. Tryggvason, Numerical simulation of the Rayleigh-Taylor instability, Journal of Computational Physics 75 (1988) 235-282.

[12] X. He, S. Chen and R. Zhang, A Lattice Boltzmann scheme for incompressible multiphase flow and its application in simulation of Rayleigh-Taylor instability, Journal of Computational Physics 152 (1999) 642-663.

[13] D. H. Rothman and J. M. Keller, Immiscible cellular-automaton fluids, J. Stat. Phys. 52 (1988) 1119-1127.

[14] A. K. Gunstensen, D. H. Rothman, S. Zaleski and G. Zanetti, Lattice Boltzmann model of immiscible fluids, Phys. Rev. A 43 (1991) 4320-4327.

[15] A. K. Gunstensen and D. H. Rothman, Microscopic modeling of immiscible fluids in three dimensions by a lattice Boltzmann method, Europhys. Lett. 18 (1992) 157-161.

[16] D. Grunau, S. Chen and K. Eggert, A lattice Boltzmann model for multiphase fluid flows, Phys. Fluids A 5 (1993) 2557.

[17] X. He, X. Shan and G. D. Doolen, A discrete Boltzmann equation model for non-ideal gases, Phys. Rev. E 57 (1998) R13.

[18] H. Chen, Discrete Boltzmann systems and fluid flows, Computer in Physics, 7(6) (1993) 632-637.

[19] R. Benzi, S. Succi and M. Vergassola, The lattice Boltzmann equation: theory and applications, Phys. Rep. 222 (1992) 145-197.

[20] S. Chen and G. D. Doolen, Lattice Boltzmann method for fluid flows, Annu. Rev. Fluid Mech. 30 (1998) 329-364.

[21] R. Zhang, X. Shan and H. Chen, Efficient kinetic method for fluid simulation beyond the Navier-Stokes equation, Phys. Rev. E 74 (2006) 046703.

[22] M. Sbragaglia, R. Benzi, L. Biferale, S. Succi, K. Sugiyama and F. Toschi, Generalized lattice Boltzmann method with multirange pseudopotential, Phys. Rev. E 75 (2007) 026702.

[23] G. Falcucci, G. Bella, G. Chiatti, S. Chibbaro, M. Sbragaglia and S. Succi, Lattice Bolzmann models with mid-range interactions, Commun. Comput. Phys. 2 (2007) 1071-1084.

[24] R. Benzi, S. Chibbaro and S. Succi, Mesoscopic lattice-Boltzmann modeling of flowing soft system, Phys. Rev. Lett. 102 (2009) 026002.

[25] G. Falcucci, S. Chibbaro, S. Succi et al., Lattice Boltzmann spray-like fluids, Europhys. Lett. 82 (2008) 24005.

[26] D. Jacqmin, Calculation of two-phase Navier-Stokes flows using phase-field modeling, Journal of Computational Physics 155 (1999) 96-127.

[27] D. H. Sharp, An overview of Rayleigh-Taylor instability, Physica D 12 (1984) 3.

[28] L. S. Luo and S. S. Girimaji, Theory of the lattice Boltzmann method: Two-fluid model for binary mixtures, Phys. Rev. E 67 (2003) 036302.

[29] W. H. Cabot and A. W. Cook, Reynolds number effects on Rayleigh-Taylor instability with possible implications for type-Ia supernovae, Nature Physics 2 (2006) 562-568.

[30] B. Cabot, A. Cook and P. Miller, Direct Numerical Simulation of Rayleigh-Taylor Instability, IWPCTM10, Paris July 2006.

[31] J. P. Wilkinson and J. W. Jacobs, Experimental study of the single-mode three-dimensional Rayleigh-Taylor instability, Phys. Fluids 19 (2007) 124102.

[32] M. Chertkov, I. Kolokolov and V. Lebedev, Effects of surface tension on immiscible Rayleigh-Taylor turbulence, Phys. Rev. E 71 (2005) 055301(R).

[33] Z. Huang, A. De Luca, T. J. Atherton, M. Bird and C. Rosenblatt, Rayleigh-Taylor instability experiments with precise and arbitrary control of the initial interface shape, Phys. Rev. Lett. 99 (2007) 204502.